Energy Transfer in the $d^3\Pi_g - a^3\Pi_u$ (0−0) Swan Bands of C_2: Implications for Quantitative Measurements†

A. Brockhinke,* M. Letzgus, S. Rinne, and K. Kohse-Höinghaus

Physikalische Chemie 1, Fakultät für Chemie, Universität Bielefeld, Universitätsstraβe 25, Bielefeld D-33615, Germany

Received: September 29, 2005; In Final Form: November 22, 2005

Energy transfer effects on dicarbon (C_2) $d^3\Pi_g \leftarrow a^3\Pi_u$ laser-induced fluorescence (LIF) spectra in fuel-rich acetylene atmospheric-pressure flames have been studied using a combination of two different two-dimensional techniques. Measurements using a picosecond laser system in conjunction with a streak camera allowed determination of typical fluorescence lifetimes of levels in the d state and of population changes introduced by rotational energy transfer (RET) and by state-dependent quenching. Excitation−emission spectroscopy yielded two-dimensional maps containing all excitation and all emission spectra in the spectral ranges between 19 340 and 20 150 cm^{-1} (excitation) and from 546 to 573 nm (emission) and allowed unambiguous assignment of all transitions in this spectral region. Our measurements show a comparatively long quenching lifetime (around 2 ns) and dominant effects of energy transfer on shape and intensity of the acquired spectra (90% of the fluorescence stems from levels populated by ET). A pronounced dependence of the total RET on the quantum number of the initially excited state is observed. Vibrational energy transfer (VET) is significantly weaker (only 5% contribution for excitation in the $v' = 1$ level). Implications for quantitative concentration measurements are discussed, and exemplary spatially resolved profiles in a well-characterized low-pressure propene flame are presented.

1. Introduction

Emissions from the carbon dimer C_2 are visible in the spectra of all carbon-containing flames. Especially the Swan bands are among the strongest bands in the visible part of the spectrum and have been assigned by King and Birge decades ago.[1] Despite this prominent visibility, the role of C_2 in flame chemistry remains unclear and is being controversially discussed. Most established mechanisms assume that the major path for C_2 formation is hydrogen abstraction from C_2H, which in turn is formed from acetylene and small polyacetylenes. This theory cannot, however, explain the isotopic patterns observed when a mixture of $^{12}C_2H_2$ and $^{13}C_2H_2$ is used as fuel. In contrast, Williams and Pasternack[2] argue that C_2 is formed by reactions of atomic carbon with CH or CH_2—an assumption that would lead to a strong correlation between the concentrations of C_2, CH and CH_2, which is not observed experimentally. Other authors[3] emphasize the possibility of C_2 formation by decomposition of large unsaturated molecules, such as oligomeric polyacetylenes. Another important open question is the role of C_2 in soot formation. Although it is commonly accepted that a large number of intermediates with low molecular weight participates in the formation of soot precursors, the role of C_2 remains undetermined. Another interesting question which may involve similar chemistry is the presence of C_2 in spectra of astrophysical origin.[4−6]

Quantitative minor species concentration measurements are a prerequisite for understanding combustion processes and pollutant formation. They are also necessary to validate and optimize reaction mechanisms and models in combustion research,[7] and recent work by Miller, Pilling and Troe has discussed the achievements and open questions of combustion kinetics in detail.[8] C_2 in flames has been detected using a wide range of techniques, including CRDS,[9,10] DFWM[11,12] and Fourier transform methods[2] as well as combinations of CRDS and LIF.[13]

Also, C_2 has been detected as a byproduct of heating carbon particles and has been used for quantitative soot volume fraction measurements.[14] Even in the UV, C_2 has been observed as a consequence of diagnostics using large laser fluences, and multiphoton transitions have been identified in sooting hydrocarbon flames.[15] However, the most important technique for quantitative, spatially resolved concentration and temperature measurements remains laser-induced fluorescence (LIF).[16−18]

The quantification of LIF measurements is, however, complicated by the fact that the measured signal strength not only is proportional to the number density in the electronic ground state but also depends strongly on electronic quenching as a function of the excited state quantum numbers and collision partner mixture. Moreover, energy transfer processes in the excited state like vibrational energy transfer (VET) and rotational energy transfer (RET) change the spectral structure of the LIF signal and frequently have a significant influence on the measured fluorescence intensity.[19] As all processes depend on the quantum states, temperature, pressure and chemical composition of the particular system studied, no general procedure to correct for their influence is available. Several experimental strategies have been suggested that might reduce the influence of collisions in the excited state, including saturated LIF and predissociative LIF.[7,20−23] However, both approaches are strongly affected by energy transfer in the ground state.[23,24] As an alternative, the use of picosecond lasers has been suggested for quench-free measurements[25−30] with the idea either to excite and detect the fluorescence in a very short time interval with

† Part of the special issue "Jürgen Troe Festschrift".

10.1021/jp055553g CCC: $33.50 © 2006 American Chemical Society
Published on Web 01/10/2006

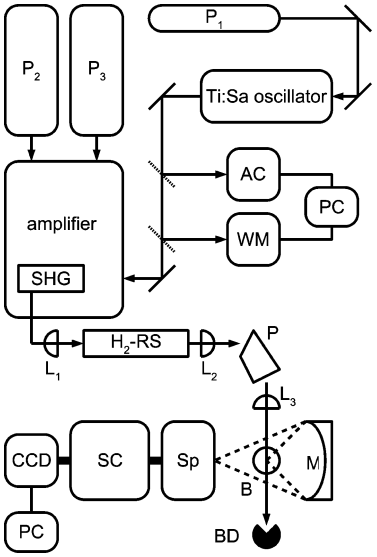

Figure 1. Experimental setup for time-resolved measurements. P_1: Ar^+ pump laser. P_2, P_3: Nd:YAG pump laser. Oscillator: mode-locked Ti: sapphire laser. AC: autocorrelator. WM: wavemeter. Amplifier: active regenerative amplifier. SHG: frequency doubling unit. L_1, L_3: 500 mm lens. L_2: 1000 mm lens. RS: Raman shifter. P: Pellin-Broca prism. B: burner (welding torch). BD: beam dump. M: mirror. Sp: spectrograph. SC: streak camera. CCD: detector camera. PC: computer.

respect to typical collision times (of the order of 100 ps in atmospheric-pressure flames) or to observe the complete temporal decay of LIF signals.

In this study, we present measurements in the C_2 $d^3\Pi_g \leftarrow a^3\Pi_u$ band system using a combination of two different two-dimensional techniques (one time-averaged, the other with picosecond temporal resolution) thereby aiming to identify processes that might affect quantitative minor species measurements. We discuss saturation, quenching and vibrational and rotational energy transfer as well as the dependence of collisionally induced processes on the quantum number of the initially excited state. Finally, we present an exemplary, quantitative, spatially resolved C_2 profile in a low-pressure propene flame and a comparison with CHEMKIN model calculations.

2. Experimental Section

2.1. Picosecond Laser System. The experimental setup for picosecond time-resolved LIF measurements is shown schematically in Figure 1. The laser system consists of a Ti:sapphire oscillator (Spectra Physics, Tsunami) and a three-stage amplifier (Spectra Physics, Model TSA-50). The oscillator is pumped by an argon ion laser and runs at a repetition rate of 80 MHz; its spectral tuning range is from 750 to 1000 nm, and several pulse durations may be selected depending on the configuration of the resonator. For the experiments described here, a pulse duration of nominally 80 ps was selected, with the resulting line width being close to the Fourier transform limit. The amplifier system consists of one regenerative amplification stage and two double-pass traveling-wave amplifiers. Two frequency-doubled Nd:YAG lasers with a 10 Hz repetition rate are used as pump sources for the amplifiers. The amplified output, also at 10 Hz repetition rate, is then frequency doubled. Finally, a Raman cell is used to shift the output radiation to the desired wavelength region around 517 nm.

The home-built Raman shifter is a steel tube of 1m length and 25 mm diameter filled with 10 bar hydrogen (Raman shift: 4155.296 cm^{-1}). The frequency-doubled laser beam is focused into the Raman cell with a 500 mm lens and collected with a 1000 mm lens. The efficiency of the conversion process is round about 20%. For wavelength separation, a Pellin-Broca prism is used.

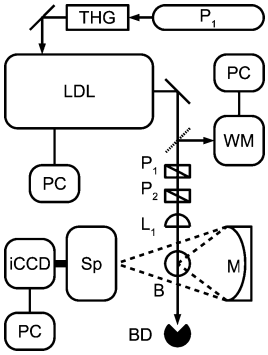

Figure 2. Experimental setup. P_1: Nd:YAG pump laser. LDL: dye laser. WM: wavemeter. P_1: Fresnel rhombus. P_2: Rochon prism. L_1: 500 mm lens. B: burner (welding torch). BD: beam dump. M: mirror. Sp: spectrograph. iCCD: detector camera. PC: computer.

The laser beam is focused into the flame using a 500 mm focal length lens. The LIF signal is collected by a large aperture (*f* number: *f*/1.0), spherical, concave mirror with Al:MgF_2 coating, in the common L-shaped setup.

For C_2 measurements, the mirror is aligned to image the laser focal region with a magnification of 2 onto the spectrograph entrance slit, which is a 275 mm focal length, *f*/4.0 aperture model (Spectra Pro 275, Acton Research) equipped with a set of three gratings mounted on a turret. In this work, the grating with 150 grooves/mm is used. The spectrograph is mounted with the entrance slit arranged parallel to the laser beam's propagation direction. The exit plane is imaged onto the entrance slit of a streak camera (Hamamatsu Model C2830) with the slit parallel to the spectral axis. On the output side of the streak camera, a gateable microchannel plate image intensifier is mounted. For the experiments described here, a streak range of nominally 10 ns has been used. The spectrally and temporally dispersed signal is ultimately detected with a cooled, slow-scan CCD camera, which provides a 12 bit dynamic range. Due to the size of the camera chip, the effective width of the streak sweep was limited to 7.6 ns. The raw data consist of two-dimensional images, where the dimensions correspond to the spatial and time scales, respectively.

2.2. Nanosecond Laser System. The experimental setup for nanosecond static LIF measurements is shown schematically in Figure 2. The dye laser (LAS LDL-205) is pumped by the third harmonic of a Nd:YAG laser (Spectra Physics DCR2A) with a repetition rate of 10 Hz and 7 ns nominal pulse duration. As in the picosecond setup the laser beam is focused into the flame with a 500 mm lens. The LIF signal is collected with a spherical mirror (*f* number: *f*/1.0) and focused on the entrance slit of the spectrometer (Spectra Pro 300i, Acton Research) with a magnification of 2. The spectrally resolved LIF signal is detected with a Peltier-cooled, intensified CCD camera with a 384 × 286 array. The signals are spectrally dispersed along the 384-pixel direction, producing a wavelength-resolved one-dimensional image of the flame. For the measurements in atmospheric-pressure flames, a MCP gate of 40 ns was used. For the quantitative measurements in low-pressure flames described in the final section, this time has been extended to 200 ns to take the longer fluorescence lifetime at reduced pressures into account.

2.3. Flame Conditions. To generate ample C_2 concentrations for the spectroscopic measurements, a standard welding torch

TABLE 1: Estimated Flame Composition for the C_2H_2/O_2 Flame Using an Adiabatic Equilibrium Calculation[32]

species, concn (%)	CO, 54.7	H_2, 27.2	N_2, 14.4
species, concn (%)	C_2H_2, 3.4	H, 0.3	other, <0.1

(Messer-Griesheim, APM GR. 3) is used. The nozzle is cooled with water to prevent overheating, which causes spontaneous decomposition of the acetylene. This decomposition leads to solid carbon plugging the nozzle and interfering with the laser beam. Additionally, the welding torch sometimes tends to blow out without cooling. It is operated with 1 slpm (standard liters per minute) of acetylene premixed with 0.83 slpm of oxygen, which equals a carbon-to-oxygen ration of C/O = 0.4 and a stoichiometry of $\phi = 3.0$. Measurements have been performed just above the inner cone of the flame at $h = 5$ mm above the nozzle. Here, C_2 emissions are strongest. Additionally, temperature and flame emissions are fairly uniform, allowing averaging over a 2 mm long region along the laser beam to improve the signal-to-noise ratio.

The flame composition is calculated by assuming adiabatic equilibrium as a first approximation. To estimate the influence of entrainment of ambient air to the premixed fuel/oxygen flow, we measured the CH radical concentration in the methane flame as function of stoichiometry. The best match between modeled and measured stoichiometry dependence was obtained at a value of 35 vol % air entrainment; details may be found in previous work.[31] Results of the calculation of the flame composition using this value are shown in Table 1. The flame temperature has been determined using the C_2 excitation−emission spectrum (EES) shown in Figure 3 by integrating the fluorescence intensity of 10 lines with different rotational quantum numbers and plotting these values vs the ground-state energy. This Boltzmann plot yielded a temperature of 2190 ± 61 K and is consistent with the level of air entrainment observed before.

3. Results

3.1. Excitation-Emission Spectra. For the LIF excitation scans, the camera is operated in the following mode: The laser is kept at a defined excitation frequency for a given number of laser pulses. At the end of this time, all signals on the array are summed along the direction of the spatial extension, retaining the spectral dispersion. This produces a one-dimensional fluorescence spectrum at this excitation frequency. After slightly changing the excitation wavelength, the process is repeated. This next fluorescence spectrum is stored next to the first one. This procedure results in a two-dimensional array, the "excitation−emission spectrum" (EES), in which the horizontal axis is excitation frequency and the vertical axis is fluorescence wavelength. One example is shown in the bottom panel of Figure 3. This kind of display, directly correlating excitation and fluorescence, greatly assists spectral identification and can, e.g., be used to identify interfering emissions as well as contributions from background emissions and nonresonant processes such as Raman scattering.[15]

The EES displayed in Figure 3 has been acquired in the spectral range between 19 340 and 19 530 cm^{-1} (excitation) and between 546 and 573 nm (emission). A conventional excitation scan has been calculated from this spectrum by integration along the fluorescence axis and is displayed in Figure 3 as well (top panel). All visible excitation lines could be assigned to transitions of the $d^3\Pi_g \leftarrow a^3\Pi_u$ (0−0) and (1−1) band system of C_2. In fluorescence, the (0−1) and (1−2) bands have been monitored. Line positions have been calculated using the data given by Lloyd and Ewart.[33]

The most intense structure is the head of the P branch at 19 355 cm^{-1}. For larger wavenumbers, rotational lines in their characteristic triplet structure are visible. One particular feature in this progression is the "staggering" effect, which is due to Λ-doubling and is commonly taken into account in simulations by using sets of different quantum mechanical constants for odd and even rotational quantum numbers, respectively.[34] Above 19 383 cm^{-1}, the R branch can be observed as well. As is typical for $^3\Pi-^3\Pi$ transitions, a Q branch is not observed at all.

In the fluorescence direction (i.e., at fixed excitation wavenumber), three strong emissions are observed. Two belong to the P and R rotational lines from the excited level. As in excitation, Q lines are not observed. For increasing rotational quantum number, the distance between the P and R lines in emission increases, forming a distinct parabolic shape that is clearly visible in Figure 3. However, the strongest feature in all fluorescence spectra is the (0−1) band head visible at 563 nm, which results from lines populated by rotational energy transfer (RET). A quantitative analysis of energy transfer effects (both RET and VET) will be presented further below.

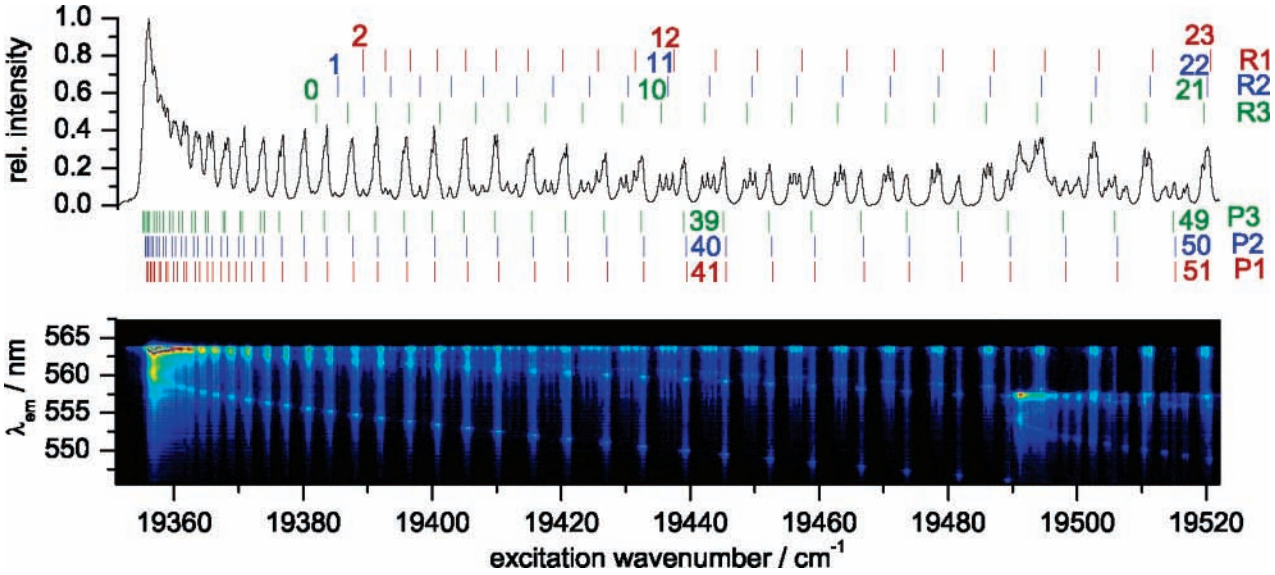

Figure 3. Conventional excitation spectrum (top) and excitation−emission spectrum (bottom) in the range between 19 340 and 19 530 cm^{-1}. All visible lines could be assigned to transitions in the $d^3\Pi_g \leftarrow a^3\Pi_u$ (0−0) and (1−1) band system of C_2.

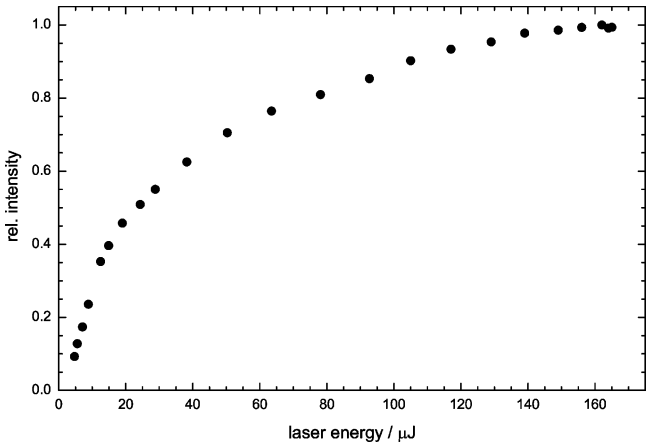

Figure 4. Power dependency of the C_2 signal for a laser beam diameter of 380 μm.

At excitation wavenumbers above 19490 cm^{-1} the (1−1) band can be excited as well and the spectrum becomes more congested. The intensity is significantly weaker, because even at flame temperatures the majority of the molecules remains in the vibrational ground state. In fluorescence, emissions from the (1−2) band are shifted by 1.8 nm toward lower wavelengths in comparison to those of the (0−1) band detected before. Again, the band head is the most prominent feature. It is located at 561.2 nm for the (1−2) band in emission. Additional EES have been measured for wavenumbers up to 20 150 cm^{-1}. All visible emissions could be unambiguously assigned to the Swan bands of C_2. Other authors[13,14] found evidence of PAH or laser-induced incandescence of soot in their C_2 spectra. We found no such contributions, probably due to the different excitation wavelengths and detection band-passes as well as the different flame composition in our investigation.

3.2. Saturation Effects. To ensure working in the linear excitation region, the power density was adjusted by combining a Fresnel rhombus and a Rochon prism. Additionally, different focusing conditions have been used to produce beam cross sections of varying diameter at the target region. This allowed a high dynamic range and reproducible adjustment of the power density over more than two decades. Figure 4 shows the power dependency of the C_2 signal for a laser beam diameter of 380 μm (excitation in the $d^3\Pi_g \leftarrow a^3\Pi_u$ (0−0) P branch head at 19 355 cm^{-1}, detection of the complete fluorescence in the (0−1) emission band). It is evident that the transition is very easy to saturate, and even at mild focusing conditions, deviations can be observed for energies above 20 μJ. This corresponds to a power density of 3.5 MW cm^{-2}, a threshold value that corresponds well to results published before.[35] In our experiments, we never observe complete saturation, probably due to spatial and temporal wing effects in the laser beam profile. To maintain an acceptable signal strength while ensuring that saturation and vaporization of soot particles do not play a significant role, the power density was kept below 3.5 MW cm^{-2} for the quantitative concentration measurements reported below.

A few decades ago, saturation spectroscopy was suggested for the detection of C_2 concentrations.[35] This approach leads, however, to two problems. The general problem of saturated LIF is the complicated quantification due to the wing effects mentioned before. Additionally, even though saturated LIF circumvents the problem of quenching and energy transfer in the excited state, rotational redistribution in the ground-state still leads to a significant effect of the collisional environment on the measured quantum efficiency. Another problem consists of the formation of C_2 by vaporization of soot particles. Dasch observed that small soot particles undergo vaporization at relatively low laser fluences (>0.2 J cm^{-2}, corresponding to 30 MW cm^{-2}).[36] Therefore, saturated LIF is not an option for quantitative measurements in sooting or near-sooting flames.

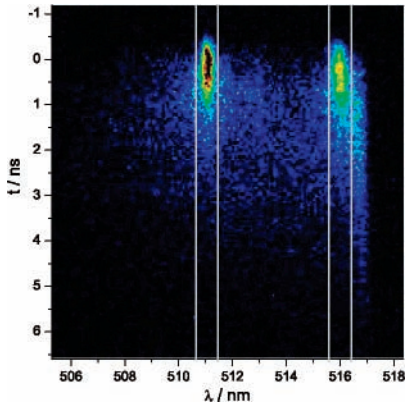

Figure 5. Raw data image from the streak camera after excitation of the triplet (0−0) $R_{11}(28)/R_{22}(27)/R_{33}(26)$. Clearly visible is the LIF from the directly populated levels and the RET populated band head. White lines indicate the boundaries of the integration ranges for the time-resolved analysis in Figure 6.

3.3. Time-Resolved Measurements. Figure 5 shows a typical raw image obtained by the streak camera. Due to the narrow line spacing in C_2 and the relatively large bandwith of the picosecond laser (≈1 cm^{-1}), all three states in one triplet are excited simultaneously. In this case, the (0−0) $R_{11}(28)/R_{22}(27)/R_{33}(26)$ transitions in the Swan bands have been probed. The vertical axis in Figure 5 shows the time succeeding the exciting laser pulse, whereas the horizontal axis corresponds to the wavelength of the detected radiation. The two bright emissions at 511 and 516 nm are due to fluorescence in the (0−0) band originating from the directly populated level, with the former being partially overlapped by Rayleigh scattered light. All other emissions visible in this image are due to fluorescence from states populated by energy transfer—a fact that is readily deduced because they reach their maximum intensity more than 1 ns after the excitation laser pulse. Especially pronounced is the P band head visible at 516.8 nm. The reason for detecting fluorescence in the (0−0) band instead of the (0−1) band used in the EES spectra is the signal-to-noise ratio: The Franck−Condon factor for the (0−0) band is more than 3 times as large as that of the (0−1) band.[37] Because Rayleigh-scattered light can easily be identified and compensated in the time-resolved spectra, this is no disadvantage for the quantitative evaluation discussed below.

For a quantitative analysis of these images, vertical profiles are taken (the integration regions are indicated in Figure 5). Figure 6 shows the corresponding temporally resolved curves, where the top panel depicts the wavelength-integrated fluorescence. In this case, the decay is dominated by quenching. To take the instrument response function and the temporal width of the laser pulse into account, a single-exponential has been fitted to the experimental curve using a deconvoluting fit algorithm.[38] Errors have been determined using a rigorous error analysis.[39] For fluorescence from the $v' = 0$ vibrational level, we determined a quenching lifetime of (2057 ± 60) ps. This is significantly longer than the quenching lifetimes of other radicals: Under the same conditions, a lifetime of 1150 ps has been measured for CH[31] and a LASKIN[40] simulation for time-resolved OH-LIF gives a quenching lifetime of 1140 ps (in this case, temperature and collisional environment have been calculated with GASEQ[41] using the NASA-method[32]).

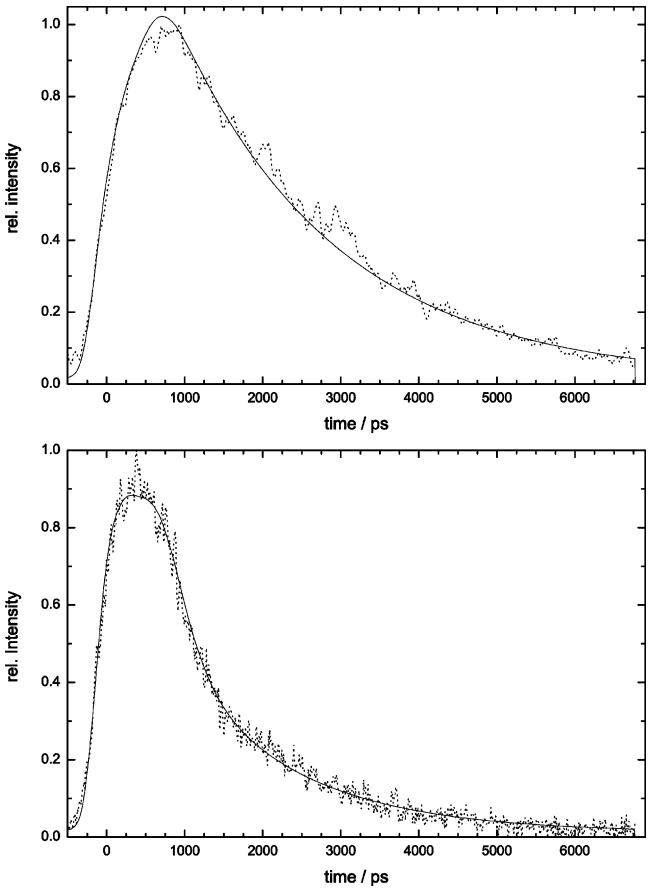

Figure 6. Time-resolved LIF after (0−0) excitation. Top panel: wavelength-integral fluorescence in the (0−0) band. Bottom panel: emission from direct populated levels (integration ranges are marked in Figure 5). Analysis is done by an iterative numerical devonvolution to obtain lifetimes.[38]

Using the known pressure and temperature a quenching rate of $k_Q = (4.9 \pm 0.2) \times 10^8$ s^{-1} or $(1.46 \pm 0.3) \times 10^{-10}$ cm^3 molecule^{-1} s^{-1} can be calculated. This value is nearly twice as large as that recently reported by Smith et al.,[42] in several hydrocarbon−air flames (8×10^{-11} cm^3 molecule^{-1} s^{-1}), but very similar to rates measured in a diamond depositing dc-arcjet (1.44×10^{-10} cm^3 molecule^{-1} s^{-1}).[43] This shows that, in contrast to the findings of Smith et al.,[42] C_2 quenching rates significantly depend on the collisional environment. Their recommendation of a fixed value seems valid only for flames of very similar chemical composition.

To extract rates for the RET process, we used an indirect method. The bottom panel of Figure 6 shows a biexponential deconvoluting fit to the decay of only the laser coupled states. Initially, the fluorescence decays very fast with a lifetime of $\tau_1 = 280 \pm 100$ ps. In contrast, the second lifetime is much slower ($\tau_2 = 1520 \pm 350$ ps). Close to the excitation laser pulse, the fluorescence decay curve will be dominated by all population removal processes: quenching, VET and RET. Re-population plays a role only at later times, because it involves several consecutive collisions. As will be shown in section 3.5, VET does not play a role in the $v' = 0$ state. Therefore, the fast initial decay will be dominated by RET. Using the simple relation $1/\tau_1 = k_Q + k_{RET}$ we determine a rate of $k_{RET} = (3.1 \pm 1.3) \times 10^9$ s^{-1} for the total RET.

It should be noted that this approach to determine the total RET rate is only a crude approximation because the decay curves might be tainted by fluorescence from adjacent levels and there might be some effects of back-transfer RET even close to the excitation laser pulse. Therefore, we describe an alternative, more accurate way to determine total RET in the next section.

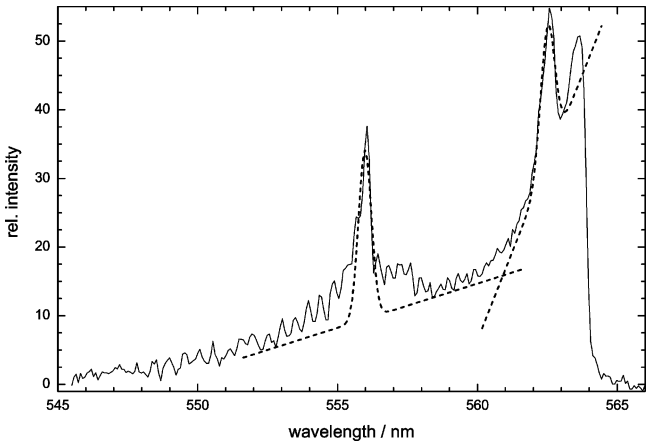

Figure 7. Illustration of the data evaluation method. To fit peaks with Gaussians, the measured spectrum must be corrected for the RET induced slope.

The same method has been applied to data measured after (1−1) excitation. Analysis of the fully wavelength-integrated decay curves yields 1715 ± 200 ps for the fluorescence decay (corresponding to a quenching rate of $k_Q = (5.8 \pm 0.7) \times 10^8$ s^{-1}). Biexponential fit of fluorescence from only the directly populated level yields lifetimes of $\tau_1 = 270 \pm 110$ ps and $\tau_2 = 1470 \pm 500$ ps. From this, the rate for the total RET can be estimated to $k_{RET} = (3.1 \pm 2.3) \times 10^9$ s^{-1}. The quenching rate is slightly higher than that measured for the $v' = 0$, whereas the rate for the total RET remains unchanged. However, the values obtained from (1−1) measurements have larger errors due to the significantly lower LIF intensities.

3.4. Rotational Energy Transfer (RET). Additional information about RET was obtained from time-integral measurements with the nanosecond laser system. Figure 7 shows a measured spectrum after (0−0) $P_{22}(27)$ (and the two adjacent triplet states) excitation. Clearly visible is the LIF signal from the directly populated states at 556 and 562.5 nm as well as the broad background with the distinct P band head at 563.8 nm caused by RET.

To determine the total fluorescence from the directly populated level, the baseline induced by RET has been approximated and subtracted and the remainder has been fitted assuming Gaussian shapes with a width determined by the spectrometer settings. This strategy already compensates for the back-transfer of population to the directly populated level by RET and is sketched in Figure 7. By comparing this value with the integral fluorescence, we can quantify the fraction of LIF from the initial level η for each spectrum. The dependence of η on the rotational quantum number is shown in Figure 8 for the C_2 $d^3\Pi_g$ $v' = 0$ state. A pronounced dependence of the total RET on the quantum number of the initially excited state is observed: for $J' < 30$ only 9% of the fluorescence stems from the directly populated level. For higher quantum numbers this fraction nearly doubles for J' around 50.

In a time-averaged spectrum, η relates to the rates for quenching k_Q and total rotational energy transfer k_{RET} by the following equation:

$$\eta = \frac{k_Q}{k_Q + k_{RET}}$$

This equation has been used to determine the rates for total

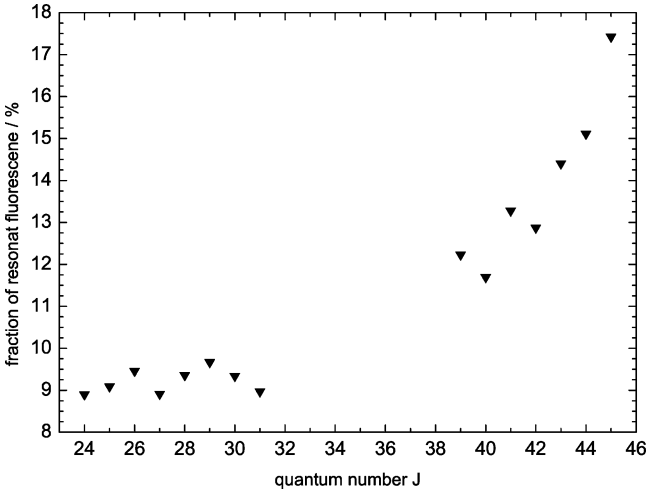

Figure 8. Dependence of the fraction of fluorescence from the directly populated level (and therefore of total RET) on the quantum number of the initially excited state for several transitions in the P band.

TABLE 2: Dependence of RET Rates on the Rotational Quantum Number in the C_2 $d^3\Pi_g$ $v' = 0$ State[a]

J'	$k/10^9$ s^{-1}	J'	$k/10^9$ s^{-1}
24	4.98	39	3.49
25	4.86	40	3.67
26	4.65	41	3.17
27	4.97	42	3.29
28	4.71	43	2.89
29	4.54	44	2.73
30	4.72	45	2.30
31	4.93		

[a] The relative error for all values is $\Delta k = 0.2 \times 10^9$.

RET listed in Table 2. Even though there is a difference in absolute values between the rates determined by the time-resolved measurements ($k_{RET} = (3.1 \pm 1.3) \times 10^9$ s^{-1}) and those determined by the procedure outlined above ($k_{RET} = (4.7 \pm 0.2) \times 10^9$ s^{-1} for values around $J' = 27$ level), they agree within the error margins. It should be noted that the method to determine RET from the static spectra is much more accurate and not as prone to systematic errors because it already takes re-population of the initially excited level into account.

3.5. Vibrational Energy Transfer (VET). In addition to rotational energy transfer, collisions might lead to a transfer of population to adjacent vibrational levels via vibrational energy transfer (VET). VET in the upward direction (i.e., with $\Delta v = +1$) is relatively weak and therefore important only for highly excited rotational states.[40] In contrast, VET toward states with lower energy ($\Delta v \leq -1$) has a much higher rate. It has been shown for OH (excitation of $A^2\Sigma^+ \leftarrow X^2\Pi$ (1−0)) that up to 30% of the fluorescence detected in time-averaged experiments is due to states populated by VET.[19]

Figure 9 shows a fluorescence spectrum detected after excitation of the P band head of the (1−1) transition at 19 490 cm^{-1}. The strong fluorescence at wavelengths below 557 nm corresponds to the (1−2) emission band and therefore originates from the directly populated vibrational level. In contrast, all emissions in the range between 558 and 563.5 nm can be attributed to the (0−1) emission band, which was populated by VET. The partial spectral overlap between the (1−2) and the (0−1) emission bands has been taken into account by extrapolating the spectral shape of the band populated by VET. Our analysis shows that the total VET in the $d^3\Pi_g$ state of C_2 under these conditions is only 5.6% and is therefore much weaker than for other small molecules. VET will be even less important

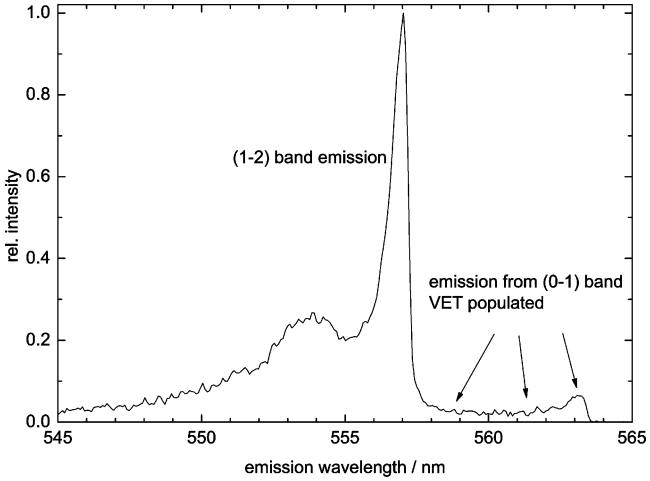

Figure 9. Fluorescence spectrum after excitation of the P band head of the (1−1) transition.

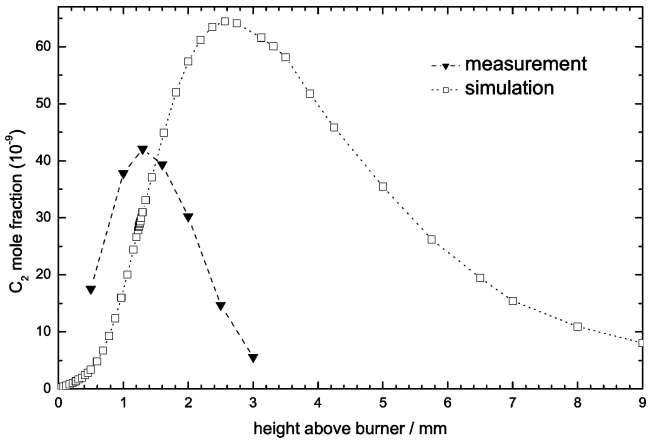

Figure 10. Absolute concentration profile of C_2 in a low-pressure propene/oxygen flame with C/O = 0.5. Solid symbols: measurements. Open symbols: comparison with a CHEMKIN II simulation using the Richter mechanism.[50]

for the $d^3\Pi_g \leftarrow a^3\Pi_u$ (0−0) transitions used for the quantitative concentration measurements described in the next section.

3.6. Flame Measurements. The energy transfer measurements in the previous sections show that C_2 in the $d^3\Pi_g$ state exhibits a relatively long quenching lifetime and the shape of the spectra is determined by fast RET. For quantitative measurements it is, therefore, necessary to integrate over a complete emission band to obtain strong signals and to minimize effects by RET. Excitation in the (0−0) band and detection in the (0−1) band is advantageous due to the high Franck−Condon factors involved,[37] the fact that VET does not play a role in the excited state and because fluorescence signals are not affected by interfering emissions and scattering processes in the (0−1) band.

Because collider-specific data are not available for C_2, simulation and compensation of energy transfer effects on quantitative measurements is not yet possible, even though the numerical models for this do exist.[40] Therefore, absolute concentration measurements by LIF are possible only if they are calibrated by a different technique. Due to the narrow width of C_2 concentration profile (see Figure 10), the collisional environment does not change significantly with height and variations of the quenching rate can be neglected.[42] The combination of the outstanding features of LIF (high spatial resolution) with those of CRDS (easier quantification due to its insensitivity to collisionally induced processes) proved to

be advantageous. This approach has already been used by other groups in different environments.[13,44]

Although a detailed inspection of the flame chemistry concerning C_2 formation and destruction is beyond the scope of this paper, quantitative C_2 concentration profiles have been exemplarily measured in a one-dimensional low-pressure propene/oxygen flame (C/O = 0.5, close to the soot formation threshold) that has already been thoroughly characterized before using a combination of optical (LIF, CRDS) and intrusive diagnostics (MBMS, molecular beam mass spectrometry using both REMPI and electron impact ionization).[45,46] For the LIF measurements it is advantageous to choose a temperature-insensitive line (in the region between 700 and 2300 K) with sufficient line strength. Spectral simulations using the equations of Phillips[34] for the line positions and of Kovacs[47] for the Hönl-London factors showed that the line triplet located at 19 376.5 cm^{-1} (consisting of the $P_{11}(28)$, $P_{22}(27)$ and $P_{33}(26)$ transitions) ideally fulfills these requirements.

For concentration measurements, the nanosecond-laser setup described in section 2.2 has been used. Fluorescence intensities have been averaged over the spectral range between 547 and 567 nm (i.e., the complete (0−1) emission band) to obtain a strong signal and are normalized to the laser energy. Absolute concentrations are calculated using CRDS calibration measurements in the same, well-characterized flame[48] using literature values of the C_2 oscillator strength.[49] With CRDS, quantitative concentrations can be determined without additional calibration measurements and without the need to take collisionally induced processes into account. However, CRDS suffers from the disadvantage of being a line-of-sight technique and has only a moderate spatial resolution. Therefore, LIF has been used to determine the centerline profile in the flame. To calculate mole fractions, the temperature profile of the flame has been taken into account.[45]

For this experiment, spatial resolution was limited by the magnification of our imaging optics and by the spectrometer slit width (750 μm) to about 0.38 mm. Figure 10 shows an absolute, spatially resolved concentration profile. The C_2 profile is very narrow with a fwhm of 0.8 mm and is nearly symmetric. This indicates that C_2 might be a good marker for the flame front. The peak mole fraction of 4.2×10^{-8} is reached relatively close to the burner surface ($h = 1.2$ mm).

For comparison, the flame has been modeled using CHEMKIN II simulations based on the Richter mechanism[50] that has been optimized to study fuel-rich chemistry (with an emphasis on precursors for aromatic hydrocarbons and soot) (see Figure 10). These simulations predict a completely different behavior with an asymmetric profile that falls off gradually after a maximum around $h = 2.4$ mm. Additionally, the observed peak mole fractions are only two-thirds of those predicted. Integrated over the complete flame this means that we measure nearly 1 order of magnitude less C_2 than predicted.

This discrepancy in shape and absolute value leads to the speculation that major C_2-decomposition paths are missing in the Richter mechanism, or that their rate constants are underpredicted. Considering the strong localization of C_2 in our profile and taking into account that CH profiles are also very narrow and close to the reaction zone, one might speculate that this is consistent with the C_2 formation mechanism suggested by Williams and Pasternack.[2] Other groups[13,42] report similar findings. However, quantitative CH measurements in the propene flame are necessary before this issue can be decided. Systematic experimental and numerical studies are currently being performed with the aim to clarify this issue.

4. Summary

Excitation−emission spectroscopy yielded two-dimensional maps containing all excitation and all emission spectra in the spectral range between 19 340 and 20 150 cm^{-1} (excitation) and 546 and 573 nm (emission) and allowed unambiguous assignment of all transitions in this spectral region to the $d^3\Pi_g \leftarrow a^3\Pi_u$ (0−0) and (1−1) Swan bands of C_2. Interference-free detection was possible in the (0−1) fluorescence band. We observe that transitions of the Swan bands are easy to saturate and that the power density has to be kept below 3.5 MW cm^{-2} to ensure working in the linear excitation regime.

Our measurements show a relatively large quenching lifetime (around 2 ns, rate $(1.46 \pm 0.3) \times 10^{-10}$ cm^3 $molecule^{-1}$ s^{-1}) and dominant effects of energy transfer on shape and intensity of the acquired spectra. A pronounced dependence of the total RET on the quantum number of the initially excited state is observed: for $J' < 30$ only 9% of the fluorescence stems from the directly populated level. For higher quantum numbers this fraction nearly doubles for J' around 50. In contrast to the strong RET, vibrational energy transfer (VET) in the $d^3\Pi_g(v' = 1)$ state of C_2 is significantly weaker. At our experimental conditions, only 5.6% of the observed fluorescence is due to levels populated by VET with $\Delta v = -1$.

Exemplary spatially resolved profiles in a low-pressure propene/oxygen flame are presented and are compared to model calculations. Significant discrepancies are observed in both the absolute values of the C_2 and the global shape of the profiles observed. Although demonstrated here for a single flame condition, this comparison suggests that C_2 chemistry is not adequately reproduced in current reaction mechanisms and either that major C_2-decomposition paths are missing or that their rate constants are significantly underpredicted. Considerably more detailed investigations are necessary, where the C_2 profiles in flames of different fuels and stoichiometries are measured. At any rate, the energy transfer studies in the present paper suggest that caution is warranted.

Acknowledgment. We thank A. Bülter for his software to simulate line positions in C_2 spectra and M. Köhler for CRDS measurements used to calibrate the concentration profiles. Support of the DFG (contract BR 1843/5-1) is gratefully acknowledged.

References and Notes

(1) King, A. S.; Birge, R. T. *Astrophys. J.* **1930**, *72*, 19−40.
(2) Williams, B. A.; Pasternack, L. *Combust. Flame* **1997**, *111*, 87−110.
(3) Gaydon, A. G. *The spectroscopy of flame*; Chapman and Hall: London, 1970.
(4) Swamy, K. S. K. *Astrophys. J.* **1991**, *373*, 266−270.
(5) Sorkhaby, O.; Blunt, V. M.; Lin, H.; Ahearn, M. F.; Weaver, H. A.; Arpigny, C.; Jackson, W. M. *Planet. Space Sci.* **1997**, *45*, 721−730.
(6) Kimata, R. S.; Izumiura, H. *Planetary Nebulae: Their Evolution and Role in the Universe*; International Astronomical Union: Paris, 2003; pp 69−70.
(7) Kohse-Höinghaus, K. *Prog. Energy Combust. Sci.* **1994**, *20*, 203−279.
(8) Miller, J. A.; Pilling, M. J.; Troe, J. *Proc. Combust. Inst.* **2005**, *30*, 43−88.
(9) Wills, J. B.; Smith, J. A.; Boxford, W. E.; Elks, J. M. F.; Ashfold, M. N. R.; Orr-Ewing, A. J. *J. Appl. Phys.* **2002**, *92*, 4213−4222.
(10) Staicu, A.; Solk, R. L.; ter Meulen, J. J. *J. Appl. Phys.* **2002**, *91*, 969−974.
(11) Kaminski, C. F.; Hughes, I. G.; Lloyd, G. M.; Ewart, P. *Appl. Phys. B* **1996**, *62*, 39−44.
(12) Nyholm, K.; Kaivola, M.; Aminoff, C. G. *Opt. Commun.* **1994**, *107*, 406−410.
(13) Mercier, X.; Therssen, E.; Pauwels, J. F.; Desgroux, P. *Proc. Combust. Inst.* **2005**, *30*, 1655−1663.
(14) Bengtsson, P. E.; Aldén, M. *Appl. Phys. B* **1995**, *60* 51−59.

(15) Brockhinke, A.; Hartlieb, A. T.; Kohse-Höinghaus, K.; Crosley, D. R. *Appl. Phys. B* **1998**, *67*, 659−665.
(16) Kohse-Höinghaus, K.; Barlow, R. S.; Aldén, M.; Wolfrum, J. *Proc. Combust. Inst.* **2005**, *30*, 89−123.
(17) *Proc. Combust. Inst.* **2002**, *29*.
(18) *Proc. Combust. Inst.* **2005**, *30*.
(19) Brockhinke, A.; Kohse-Höinghaus, K. *Faraday Discuss.* **2001**, *119*, 275−286.
(20) Andresen, P.; Bath, A.; Gröger, W.; Lülf, H. W.; Meijer, G.; ter Meulen, J. J. *Appl. Opt.* **1988**, *27*, 365−378.
(21) Eckbreth, A. C. *Laser Diagnostics for Combustion Temperature and Species*, 2nd ed.; Abacus Press: Cambridge, MA, 1996.
(22) Rothe, E.; Gu, Y.; Chryssostomou, A.; Andresen, P.; Bormann, F. *Appl. Phys. B* **1998**, *66*, 251.
(23) Daily, J. W.; Rothe, E. W. *Appl. Phys. B* **1999**, *68*, 131−140.
(24) Kliner, A.; Farrow, R. *J. Chem. Phys.* **1999**, *110*, 412.
(25) Linne, M. A.; Brockhinke, A. Short-pulse techniques: Picosecond fluorescence, energy transfer and 'quench-free' measurements. In *Applied Combustion Diagnostics*; Kohse-Höinghaus, K., Jeffries, J. B., Eds.; Taylor and Francis: New York, 2002; Chapter 5, pp 128−154.
(26) Dreizler, A.; Tadday, R.; Monkhouse, P.; Wolfrum, J. *Appl. Phys. B* **1993**, *57*, 85.
(27) Köllner, M.; Monkhouse, P. *Appl. Phys. B* **1995**, *61*, 499−503.
(28) Bormann, F.; Nielsen, T.; Burrows, M.; Andresen, P. *Appl. Phys. B* **1996**, *62*, 601.
(29) Renfro, M. W.; Pack, S. D.; King, G. B.; Laurendeau, N. M. *Appl. Phys. B* **1999**, *69*, 137.
(30) Brockhinke, A.; Bülter, A.; Rolon, J.-C.; Kohse-Höinghaus, K. *Appl. Phys. B* **2001**, *72*, 491−496.
(31) Bülter, A.; Rahmann, U.; Brockhinke, A.; Kohse-Höinghaus, K. *Appl. Phys. B* **2004**, *79*, 113−120.
(32) Gordon, S.; McBride, B. J. Computer Program for Calculation of Complex Chemical Equilibrium Compositions, and Applications. NASA RP-1311, 1994.
(33) Lloyd, G. M.; Ewart, P. *J. Chem. Phys.* **1999**, *110*, 385−392.
(34) Phillips, J. G. *J. Mol. Spectrosc.* **1968**, *28*, 233−242.
(35) Baronavski, A. P.; Mcdonald, J. R. *Appl. Opt.* **1977**, *16*, 1897−1901.
(36) Dasch, C. J. *Appl. Opt.* **1984**, *23*, 2209−2215.
(37) Danylewych, L. L.; Nicholls, R. W. *Proc. R. Soc. London A* **1974**, *339*, 197−212.
(38) Letzgus, M. *FINDFIT*- -Fast Iterative Numerical Deconvolution; University of Bielefeld, Faculty of Chemistry, Physical Chemistry I, 2005.
(39) Lakowicz, J. R. *Principles of Fluorescence Spectroscopy*, 2nd ed.; Kluwer Academic/Plenum Publishers: New York, 1999; pp 122−124.
(40) Rahmann, U.; Bülter, A.; Lenhard, R.; Düsing, R.; Markus, D.; Brockhinke, A.; Kohse-Höinghaus, K. LASKIN − A Simulation Program for Time-Resolved LIF-Spectra, Internal Report. University of Bielefeld, Faculty of Chemistry, Physical Chemistry I, http://pc1.uni-bielefeld.de/laskin, 2003.
(41) Morley, C. GASEQ − A Chemical Equilibrium Program for Windows, http://www.gaseq.co.uk/, 2005.
(42) Smith, G. P.; Park, C.; Schneiderman, J.; Luque, J. *Combust. Flame* **2005**, *141*, 66−77.
(43) Luque, J.; Juchmann, W.; Jeffries, J. B. *J. Appl. Phys.* **1997**, *82*, 2072−2081.
(44) Luque, J.; Berg, P. A.; Jeffries, J. B.; Smith, G. P.; Crosley, D. R.; Scherer, J. J. *Appl. Phys. B* **2004**, *78*, 93−102.
(45) Kohse-Höinghaus, K.; Schocker, A.; Kasper, T.; Kamphus, M.; Brockhinke, A. *Z. Phys. Chem.* **2005**, *219*, 583−599.
(46) Kohse-Höinghaus, K.; Atakan, B.; Lamprecht, A.; Alatorre, G. G.; Kamphus, M.; Kasper, T.; Liu, N. N. *Phys. Chem. Chem. Phys.* **2002**, *4*, 2056−2062.
(47) Kovacs, I. *Astrophys. J.* **1966**, *145*, 634−647.
(48) Schocker, A.; Kohse-Höinghaus, K.; Brockhinke, A. *Appl. Opt.* **2005**, *44*, in press.
(49) Wills, J. B.; Smith, J. A.; Boxford, W. E.; Elks, J. M. F.; Ashfold, M. N. R.; Orr-Ewing, A. J. *J. Appl. Phys.* **2002**, *92*, 4213−4222.
(50) Richter, H.; Howard, J. B. *Phys. Chem. Chem. Phys.* **2002**, *4*, 2038−2055.